International Journal of Multiphase Flow 58 (2014) 39–51

Contents lists available at ScienceDirect

International Journal of Multiphase Flow

journal homepage: www.elsevier.com/locate/ijmulflow

Optimization of capillary flow through square micropillar arrays

R.S. Hale [a], R.T. Bonnecaze [b], C.H. Hidrovo [a,*]

[a] Multiscale Thermal Fluids Laboratory, Department of Mechanical Engineering, The University of Texas, Austin, TX, USA
[b] Department of Chemical Engineering, The University of Texas, Austin, TX, USA

ARTICLE INFO

Article history:
Received 18 September 2012
Received in revised form 13 August 2013
Accepted 14 August 2013
Available online 28 August 2013

Keywords:
Capillary flow
Wicking
Micropillar
Permeability
Heat pipe

ABSTRACT

This work compares several models for fluid flow through micropillar arrays to numerical simulations and uses them to optimize pillar dimensions for maximum fluid flow in a heat pipe application. Micropillar arrays are important for controlling capillary flow in microfluidic devices, and array permeability is a key parameter in determining fluid flow rate. Several permeability models are considered, including the Brinkman equation, numerical simulations, inverse reciprocal sums of a cylinder bank and open flow over a flat plate, and an analytical solution developed by the authors derived from a 2-dimensional velocity profile with appropriately varying boundary conditions. The comparison seeks to identify the models that are reliable over a wide range of porosities yet flexible enough to accommodate new pillar configurations. Numerical simulations of pillar permeability are the most desirable due to their accuracy. For pillars arranged in a square pattern, the 2-D analytical solution proposed in this study performs well at short pillar heights while the Brinkman equation is more accurate at tall pillar heights. Therefore, a hybrid model is formulated that uses the 2-D solution for $h/d \leqslant 5$ and the Brinkman model for $h/d > 5$. The 2-D solution, the Brinkman equation using specifically the permeability derived by Tamayol and Bahrami (2009), and numerical simulations are easily adapted to alternative pillar arrangements. A comparison of these models for pillars arranged in a rectangular pattern demonstrated that the authors' proposed solution is an excellent match to numerical results. These findings are applied to capillary fluid flow in heat pipes to explore the effects of pillar spacing, diameter, and height on the maximum fluid flow rate through the wick. At a given height aspect ratio, there is an optimum pillar spacing that balances the viscous losses and driving capillary pressure such that the flow rate reaches a maximum. In addition, the flow rate is increased by increasing pillar height if the pillar spacing is maintained at the corresponding optimum point.

1. Introduction

Microscale pillar arrays have received extensive attention due to their applicability to a wide range of technologies. Lab-on-a-chip systems have used pillar arrays for high-performance liquid chromatography (de Beeck et al., 2012; Song et al., 2012), dielectrophoresis (Cui and Lim, 2009), and isolating cancer cells (Nagrath et al., 2007; Sheng et al., 2012). Thermal management is another area of interest, where pillars have recently been studied for use in a flat plate heat pipe (Lips et al., 2010; Nam et al., 2010; Lefevre et al., 2012). One of the key parameters of interest for these technologies is the macroscopic rate of fluid flow through the array. The flow rate is dictated by the balance of the permeability and capillary forces of the pillar array. Small pore radii result in large driving capillary pressures but decrease permeabilities. Therefore, the ability to accurately predict the permeabilities of pillar arrays is crucial to their design and utilization.

Sangani and Acrivos (1982) studied the viscous permeability of square and hexagonal cylinder arrays at high and low porosity limits. Drummond and Tahir (1984) modeled flow around long fibers using a cell approach to find permeabilities at high porosities. Gebart (1992) used the lubrication approximation for transverse flow through square and hexagonal cylinder arrays to find an expression for the permeability at low porosities. Yazdchi et al. (2011) compiled a summary of cylinder array permeability models and compared them to finite element simulations, then created a hybrid equation valid for all porosities based on Gebart (1992) and Drummond and Tahir (1984). Yazdchi et al. (2012) later extended the finite element simulations to investigate random cylinder arrays. Tamayol and Bahrami (2009) and Zhang et al. (2010) used cell approaches to model actual pillar arrays as opposed to long cylinder arrays. Xiao and Wang (2011) and Byon and Kim (2011) used the Brinkman equation for flow through porous media to find an analytical solution for permeability. Tamayol et al. (2013) calculated the pressure drop for flow through

* Corresponding author. Tel.: +1 5122320865.
E-mail address: hidrovo@mail.utexas.edu (C.H. Hidrovo).
URL: http://www.me.utexas.edu/~hidrovo (C.H. Hidrovo).

0301-9322/$ - see front matter © 2013 Elsevier Ltd. All rights reserved.
http://dx.doi.org/10.1016/j.ijmultiphaseflow.2013.08.003

a microchannel filled with a pillar array. Their method used the Brinkman equation and resulted in a hyperbolic solution. Finally, Srivastava et al. (2010) used numerical simulations to develop a predictive equation for the volumetric flow rate of liquid through a limited range of pillar geometries, and Ranjan et al. (2012) used numerical simulations to develop correlations for pillar array permeability as a function of porosity for different pillar shapes.

These models have yet to be compared side-by-side. Srivastava et al. (2010), Ranjan et al. (2012), and Yazdchi et al. (2011) demonstrated the use of state-of-the-art numerical simulations which give exact predictions of pillar systems. In addition, the models of cylinder banks by Gebart (1992), Drummond and Tahir (1984), and Sangani and Acrivos (1982) are excellent analytical solutions for the porosity regimes in which they were developed. Alternatively, Tamayol and Bahrami (2009) and Zhang et al. (2010) proposed approximate analytical solutions which are more easily manipulated to reflect changes in pillar geometry. The design of micropillar wicks requires a robust model that applies to all porosities, yet is flexible enough to allow rapid testing of new ideas. This study seeks to identify such a model from the current approaches.

Since the permeability of a pillar array is solely a function of pillar geometry, researchers can customize flow rate predictions to their specific application with the capillary pressure drop. Some applications require fluid to move as a liquid propagation front, others as a continuous flow. Liquid front propagation technologies have pressure drops that relate to surface energies and dynamic meniscus shapes (Ishino et al., 2007; Xiao et al., 2010; Xiao and Wang, 2011). Continuous flow technologies have pressure drops that rely primarily on the effects of pillar geometry on meniscus shape (Peterson, 1994; Lips et al., 2010; Ranjan et al., 2012). Here we are interested in the particular application of flat plate heat pipes (FPHP) with microstructured wicks for thermal management.

Heat pipes are cooling devices that utilize passive capillary fluid flow through internal wicking structures to remove heat via a phase change process in a closed system. Wang and Bar-Cohen (2007) concentrated on the need for on-chip cooling technologies to combat hot spots on silicon chips. Therefore, small size and uncomplicated operation is desirable for electronic cooling. Micropillar arrays have the potential to contribute in this area, but the majority of recent modeling work has focused on liquid front propagation technologies. Lips et al. (2010) characterized the liquid–vapor interface of fluid flow through 2-D wicking structures in FPHP with confocal microscopy, and Lefevre et al. (2012) expanded the work to include meniscus curvature measurements along the length of the heat pipe. One of their wicking structures consisted of rectangular micropillars arranged in a square pattern. Sharratt et al. (2012) investigated the phase change heat transfer performance of copper micropillars arranged in several different geometric designs. We seek to optimize pillar array dimensions to achieve maximum fluid flow through a micropillar wick for heat pipe applications.

2. Fluid flow models

Imagine an array of pillars with diameter d, height h, edge-to-edge distance in the y-direction w, edge-to-edge distance in the x-direction s, and center-to-center distance in the x-direction $l = w + d$ (Fig. 1). For a square pattern, $w = s$. Fluid flow occurs in the x-direction, and the liquid interface at h is assumed to be flat. A few recent studies have included the effects of meniscus shape on permeability (Xiao et al., 2010; Xiao and Wang, 2011; Byon and Kim, 2011), but the interface was kept flat in this study to compare across a broader range of modeling work. This study will only consider an array unbounded by macroscopic sidewalls, but Vangelooven and Desmet (2010) have pointed out that the sidewalls of a bounded array must be carefully placed to avoid discrepancies between the bulk velocity and the edge velocity.

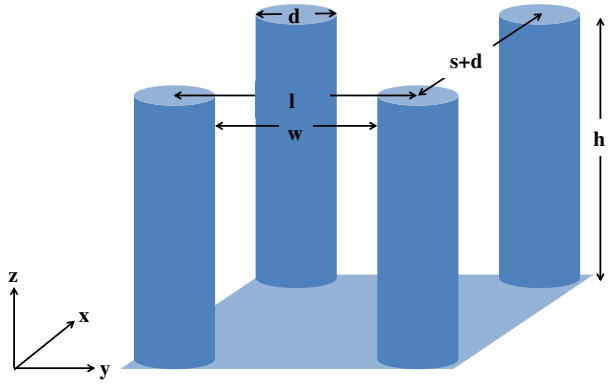

Fig. 1. Micropillar unit cell with geometric parameters. Fluid flow is in the x-direction.

If the pressure gradient is assumed to be constant and is applied only in the x-direction, the Darcy fluid flow model states that the superficial fluid velocity U is related to the pressure gradient across the system dP/dx such that

$$U = -\frac{dP}{dx}\frac{K}{\mu}, \tag{1}$$

where K is the sample permeability and μ is the fluid viscosity. The permeability is commonly non-dimensionalized by the pillar diameter, such that $K^* = K/d^2$. Thus, calculating the mass flow rate through a micropillar array requires knowledge of the dimensionless permeability.

2.1. Cylinder bank and flat plate combination

One approach to calculating the permeability through a micropillar array is to combine the permeability of an unbounded cylinder bank with the permeability of a flat plate by assuming a constant superficial velocity through the array and utilizing the fact that total pressure drop is equal to the sum of the individual component pressure drops:

$$U = -\left(\frac{dP_{cyl}}{dx}\right)\frac{K_{cyl}}{\mu} = -\left(\frac{dP_{plate}}{dx}\right)\frac{K_{plate}}{\mu} \tag{2}$$

$$\left(\frac{dP_{total}}{dx}\right) = \left(\frac{dP_{cyl}}{dx}\right) + \left(\frac{dP_{plate}}{dx}\right). \tag{3}$$

Solving Eq. (2) and (3) simultaneously gives

$$K^*_{total} = \left(\frac{1}{K^*_{cyl}} + \frac{1}{K^*_{plate}}\right)^{-1}, \tag{4}$$

which weights each individual permeability such that the total permeability automatically reflects the dominance of either the flat plate or cylinder bank characteristics of the array. The permeability of a flat plate is derived from steady, laminar flow driven by a constant pressure gradient and having no-slip and free surface boundary conditions at $z = 0$ and $z = h$, respectively (Deen, 1998):

$$K_{plate} = \frac{1}{3}h^2\epsilon. \tag{5}$$

The 2-dimensional porosity, ϵ (Eq. (6)), accounts for the fact that Eq. (1) refers to superficial velocity.

$$\epsilon = 1 - \frac{\pi}{4}\frac{d^2}{l^2}. \tag{6}$$

Since d is the parameter chosen for non-dimensionalization, Eq. (7) gives the final result for K^*_{plate} even though d does not have a direct physical meaning for a plate without pillars.

$$K^*_{plate} = \frac{1}{3}\left(\frac{h}{d}\right)^2 \epsilon. \tag{7}$$

The permeability of a square cylinder bank (also referred to as a periodic fibrous porous media in the literature) has been calculated by several researchers using a variety of techniques. Yazdchi et al. (2011) provided a synopsis of the most well-known models and their methods. His finite element model matched that of Gebart (1992) at low porosities and those of Drummond and Tahir (1984) and Sangani and Acrivos (1982) at high porosities. In addition, Shou et al. (2011) recently published another model for the permeability of fibrous porous media when $\epsilon > 0.7$ that also matched that of Yazdchi et al. (2011).The non-dimensional permeability $K^*_{G,cyl}$ given by Gebart (1992) is

$$K^*_{G,cyl} = \frac{4}{9\pi\sqrt{2}}\left(\sqrt{\frac{1-\epsilon_c}{1-\epsilon}} - 1\right)^{5/2}, \tag{8}$$

where $\epsilon_c = 1 - \pi/4$. The permeability by Drummond and Tahir (1984) $K^*_{D,cyl}$ in terms of solid fraction ϕ is

$$K^*_{D,cyl} = \frac{1}{32\phi}\left(\ln\left(\frac{1}{\phi}\right) - 1.476 + \frac{2\phi - 0.796\phi^2}{1 + 0.489\phi - 1.605\phi^2}\right), \tag{9}$$

where $\phi = 1 - \epsilon$. Yazdchi et al. (2011) proposed a combination of these two models that is valid for all porosities, given in Eqs. (10)–(12):

$$K^*_{Y,cyl} = K^*_{G2} + \left(K^*_{D,cyl} - K^*_{G2}\right)m(\epsilon), \tag{10}$$

$$K^*_{G2} = \frac{K^*_{G,cyl}}{1 + 0.336(\epsilon - \epsilon_c)}, \tag{11}$$

$$m(\epsilon) = \frac{1 + \tanh\left(\frac{\epsilon - \epsilon_h}{\epsilon_t}\right)}{2}, \tag{12}$$

where $\epsilon_h = 0.75$ and $\epsilon_t = 0.037$.

Finally, Tamayol and Bahrami (2009) assumed a parabolic velocity profile for fluid flow in fibrous porous media with velocity varying only in the y-direction. The fiber array was split into unit cells, and the velocity at the cell boundaries varied linearly from zero at the fiber surface to a maximum value in the middle of the cell. The maximum value depended linearly upon the porosity of the entire fiber array. The resulting equation for dimensionless permeability through a square array of fibers is

$$K^*_{T,cyl} = \left\{\frac{18 + 12(\eta - 1)}{\sqrt{\eta}(1-\eta)^2} + \frac{18\sqrt{\eta}\left[\arctan\left(\frac{1}{\sqrt{\eta}-1}\right) + \pi/2\right]}{(\eta-1)^{5/2}} + \frac{12(\sqrt{\eta}-1)}{\eta\sqrt{\eta}}\left[\frac{2 - g(\epsilon)}{2}\right]\right\}^{-1}, \tag{13}$$

where η is related to the solid fraction ϕ by the equation $\eta = \pi/(4\phi)$. $g(\epsilon)$ contributes to the border velocity and is given by

$$g(\epsilon) = 1.274\epsilon - 0.274. \tag{14}$$

Eq. (13) can also be written in terms of separate x- and y-direction pillar spacings, such that the pillars are arranged in rectangular patterns. Using the relationship $S = s + d$, the result of this distinction is Eq. (15):

$$K^*_{T,cyl} = \left\{\frac{18d^3 + 12d(S^2 - d^2)}{(d^2 - l^2)^2 S} + \frac{18d^4 l^2\left[\arctan\left(\frac{d}{\sqrt{l^2 - d^2}}\right) + \pi/2\right]}{(l^2 - d^2)^{5/2} S} + \frac{12(S-d)d^2}{l^2 S}\left[\frac{2 - g(\epsilon)}{2}\right]\right\}^{-1}. \tag{15}$$

Using Eq. (4) to combine the dimensionless permeabilities proposed by either Yazdchi et al. (2011) or Tamayol and Bahrami (2009) with the permeability of a flat plate gives two different models for the total permeability of a micropillar array: $K^*_{Y,total}$ and $K^*_{T,total}$.

2.2. Brinkman equation

Another method of modeling fluid flow through micropillar arrays is to use the 1-D form of the Brinkman equation. The Brinkman equation is a modified form of the Navier–Stokes equation that accounts for the permeability of a porous media:

$$\mu\frac{d^2u}{dz^2} - \epsilon\frac{dP}{dx} - \mu\alpha^2\epsilon u = 0, \tag{16}$$

where $1/\alpha^2$ is equal to the permeability of an infinite cylinder bank, generally selected from literature. This permeability must be derived from a cylinder bank arranged in the same pattern and subject to the same flow conditions as the desired micropillar system. This presents a challenge for non-standard pillar configurations since the majority of researchers have only studied square or hexagonal arrays. Xiao et al. (2010) used the permeability of Sangani and Acrivos (1982) in their work, but this study uses that of Yazdchi et al. (2011) since it is applicable to all porosities and has been validated against Sangani and Acrivos (1982) and others. Xiao et al. (2010) solved the Brinkman equation for a square micropillar array, resulting in the following velocity profile:

$$u = Ae^{\alpha\sqrt{\epsilon}z} + Be^{-\alpha\sqrt{\epsilon}z} - \frac{1}{\alpha^2\mu}\frac{dP}{dx}, \tag{17}$$

$$A = \frac{dP}{dx}\frac{\exp(-\alpha h\sqrt{\epsilon})}{\alpha^2\mu\left[\exp(\alpha h\sqrt{\epsilon}) + \exp(-\alpha h\sqrt{\epsilon})\right]}, \tag{18}$$

$$B = \frac{dP}{dx}\frac{\exp(\alpha h\sqrt{\epsilon})}{\alpha^2\mu\left[\exp(\alpha h\sqrt{\epsilon}) + \exp(-\alpha h\sqrt{\epsilon})\right]}. \tag{19}$$

Integrating Eq. (17) from 0 to h gives the average fluid velocity and subsequently the dimensionless permeability as defined by Eq. (1), which is

$$K^*_B = \frac{1}{\alpha^2 d^2} + \frac{\mu}{-\frac{dP}{dx}d^2 h}\left[\frac{A}{\alpha\sqrt{\epsilon}}\left(e^{\alpha\sqrt{\epsilon}h} - 1\right) - \frac{B}{\alpha\sqrt{\epsilon}}\left(e^{-\alpha\sqrt{\epsilon}h} - 1\right)\right]. \tag{20}$$

2.3. 2-D solution

Zhang et al. (2010) expanded the Navier–Stokes equation to account for velocity variations in both the y- and z-directions. They used a cell approach to divide the pillar array into two sections: with and without pillars. The section without pillars is called section A, and the section with pillars is called section B. The section domains are shown in Fig. 2. Section A used the same solution as a flat plate. Section B approximated the pillar surfaces as rectangular plates of height h and length d, then used the Navier–Stokes equation to solve for the velocity profile. The authors have improved this model by accounting for the actual area available for flow in the pillar region as a function of x, and by changing the boundary conditions in the section without pillars to account for developing flow behavior.

Continuity is maintained by assuming a constant superficial velocity throughout both sections. The pressure drops across section A and section B are added together to determine the total pressure drop. The full wick contains multiple cells, so we multiply the individual cell pressure drops by the number of cells in a given wick length L to determine the total pressure drop:

$$\Delta P_{total} = (\Delta P_{A,cell} + \Delta P_{B,cell})\left(\frac{L}{s+d}\right). \tag{21}$$

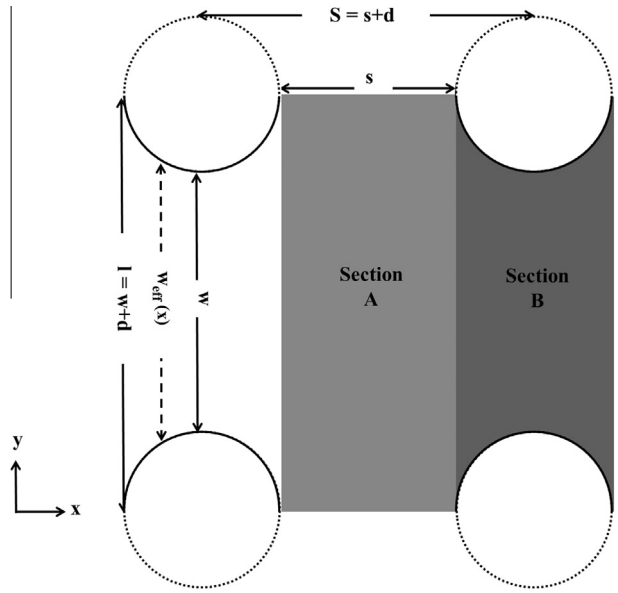

Fig. 2. Top-down schematic of pillar array to illustrate sections used in proposed 2-D model.

The governing equation is

$$\frac{dP}{dx} = \mu\left(\frac{\partial^2 u}{\partial y^2} + \frac{\partial^2 u}{\partial z^2}\right). \tag{22}$$

This requires a finite Fourier transform solution, as described in detail by Deen (1998). The non-dimensional parameters are

$$\bar{z} = z/h; \quad \bar{y} = y/l; \quad \bar{u} = \frac{u}{-\frac{dP}{dx}\frac{h^2}{2\mu}}; \quad a = h/w_{eff}; \tag{23}$$

where w_{eff} is the effective width of the channel available for flow. In section A, $w_{eff} = l$, but in section B, w_{eff} varies between l and w as a function of x. The z-direction boundary conditions are no-slip at $\bar{z} = 0$ and free shear at $\bar{z} = 1$. The boundary conditions at $\bar{y} = 0$ and $\bar{y} = 1$ depend on whether we are considering section A or section B. The boundary conditions will be zero shear stress in section A and zero velocity (no-slip) in section B. They are represented generically here as a boundary velocity condition $\bar{u}_b$ and will be further defined in the following sections. Fig. 3 gives a visual depiction of the mathematical domain.

The non-dimensional solution to Eq. (22) is

$$\bar{u} = \sum_{n=0}^{\infty} \sin(\lambda_n \bar{z}) \left\{ \left(\frac{4\bar{u}_b - 4}{\lambda_n^3}\right) \left(\frac{\sinh\frac{\lambda_n}{a}\bar{y} + \sinh\frac{\lambda_n}{a}(1-\bar{y})}{\sinh\frac{\lambda_n}{a}}\right) + \frac{4}{\lambda_n^3} \right\}, \tag{24}$$

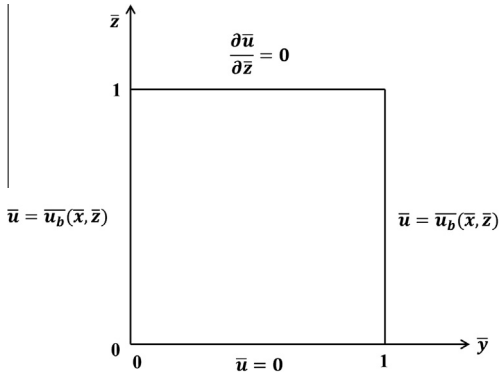

Fig. 3. Finite Fourier transform domain for 2-D velocity solution.

where $\lambda_n = (n + 1/2)\pi$. The infinite summation was truncated at either 20 or 100 terms, depending on the value of a. From this solution, the average dimensionless velocity $\bar{u}_{avg}$ arises from integrating the velocity across the flow area and dividing by the total area. So, the superficial dimensional velocity becomes

$$U = \bar{u}_{avg}\left(\frac{-h^2}{2\mu}\frac{dP}{dx}\right)\left(\frac{w_{eff}}{l}\right). \tag{25}$$

2.3.1. Section A

The pressure drop for section A depends on the boundary conditions at $\bar{y} = 0$ and $\bar{y} = 1$. The boundaries are symmetric, but this model also requires the velocity conditions at the boundary. One approach is to assume fully developed flow so that the velocity profile is uniform in the y-direction. This means that the flow jumps immediately from no-slip on the cylinder wall to a fully developed profile at the beginning of section A, which would result in an upper bound estimate for the final permeability. The opposite approach is to assume that the velocity remains zero along the entire boundary, which would provide a lower bound estimate for the final permeability. A third approach is to specify a velocity profile at the boundary that falls between these two extremes. These simplified approaches allow us to calculate the limiting cases of this model as well as a midrange solution with flexible, analytical equations that clearly display the individual effects of x- and y-direction pillar spacings. To create a generic equation for all three of these cases, we first choose the shape of the boundary velocity profile in the z-direction to match a fully developed flow profile, *i.e.* parabolic with a set velocity at the liquid surface, u_s. The boundary velocity is

$$\bar{u}_b = \bar{u}_s(2\bar{z} - \bar{z}^2). \tag{26}$$

The value of $\bar{u}_s$ dictates which approach is being used. For the first case, setting $\bar{u}_s = 1$ creates a uniform velocity profile equal to fully developed flow over a flat plate. Setting $\bar{u}_s = 0$ for the second case maintains a zero velocity condition at the boundary. For the last case, the surface velocity is given a finite value between 0 and 1. Fig. 4 shows the 3-D profile of $\bar{u}$ (Eq. (24)) vs. $\bar{y}$ and $\bar{z}$ for the three cases. The bottom profile uses an arbitrary value of $\bar{u}_s = 0.2$ to demonstrate the general profile shape. In reality, the value of $\bar{u}_s$ depends on x and has been chosen to increase parabolically from zero at the cylinder wall to some maximum value ($\bar{u}_{max}$) at the midpoint between pillars before returning to zero again at the next set of pillars. The three possible values for $\bar{u}_s$ are summarized here:

$$\bar{u}_s = \begin{cases} 1 & \text{Fully dev. velocity profile at boundary} \\ 0 & \text{Zero velocity at boundary} \\ 4\bar{u}_{max}(\bar{x} - \bar{x}^2) & \text{Varying velocity profile at boundary} \end{cases} \tag{27}$$

The dimensionless value for $\bar{x}$ goes from 0 to 1 across section A. $\bar{x} = 0$ occurs at the trailing edge of the first set of pillars ($x = d$), and $\bar{x} = 1$ occurs at the leading edge of the next set of pillars ($x = s + d$). The maximum velocity $\bar{u}_{max}$ is reached midway between pillars and is a function of S-spacing, such that pillars spaced further apart achieve a higher velocity at the midpoint than pillars spaced closer together. The dependence of $\bar{u}_{max}$ on S-spacing chosen for this model is

$$\bar{u}_{max} = \begin{cases} 0 & \text{for } S/d < 4.5 \\ -0.00238\left(\frac{S}{d}\right)^2 + 0.119\frac{S}{d} - 0.487 & \text{for } 4.5 \leqslant S/d \leqslant 25 \\ 1 & \text{for } S/d > 25 \end{cases} \tag{28}$$

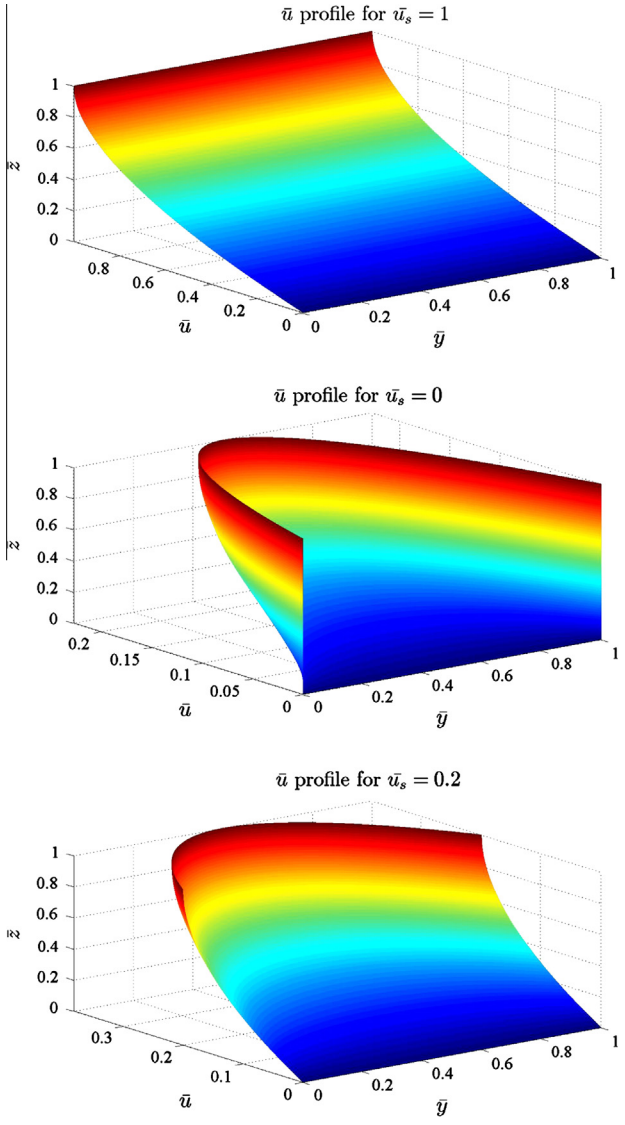

Fig. 4. Dimensionless velocity profiles (Eq. (24)) for flow with three different y-direction boundary conditions: $u_s = 1$ (top), $u_s = 0$ (center), $u_s = 0.2$ (bottom).

The piece-wise function for $\bar{u}_{max}$ stems from COMSOL V4.3 simulation results (COMSOL, Inc., Stockholm, Sweden), which will be discussed more thoroughly in the next section. COMSOL simulations matched the solution $\bar{u}_s = 0$ most closely until S/d became greater than ~4.5. Above $S/d \sim 4.5$, comparisons of the model results with COMSOL simulations indicated that the best match occured when $\bar{u}_{max}$ increased parabolically with S/d. The maximum velocity should reach 1 at large values of S/d, so as a first approximation we assume that $\bar{u}_{max} = 0$ at $S/d = 4.5$ and increases parabolically to $\bar{u}_{max} = 1$ at an arbitrarily large value of $S/d = 25$ ($\epsilon = 0.9987$). For section A, $w_{eff} = l$ and Eq. (25) becomes

$$U = \bar{u}_{avg}\frac{-h^2}{2\mu}\frac{dP_{A,cell}}{dx}. \tag{29}$$

The fully developed flow case ($\bar{u}_s = 1$) leads to the standard equation for laminar flow over a flat surface. Eq. (25) simplifies to

$$U_{(\bar{u}_s=1)} = \frac{-h^2}{3\mu}\frac{dP_{A,cell}}{dx}. \tag{30}$$

Assuming that dP/dx is constant, integrating from $x = d$ to $x = S$ gives the pressure drop across section A for single cell. Scaling by the total number of cells in an array produces

$$\Delta P_{A,(\bar{u}_s=1)} = \frac{3\mu}{h^2}\left(\frac{s}{s+d}\right)LU. \tag{31}$$

The assumption of zero velocity at the boundaries ($\bar{u}_s = 0$) makes $\bar{u}_{avg}$ independent of x, so

$$\Delta P_{A,(\bar{u}_s=0)} = \frac{2\mu}{h^2}\frac{1}{\bar{u}_{avg}}\left(\frac{s}{s+d}\right)LU, \quad \text{where } \bar{u}_s = 0. \tag{32}$$

The last case of a varying boundary velocity makes $\bar{u}_{avg}$ a function of x, since $\bar{u}_s$ is a function of x. Therefore,

$$\Delta P_{A,(\bar{u}_s=f(\bar{x}))} = \frac{2\mu}{h^2}\frac{LU}{s+d}\int_d^{s+d}\frac{1}{\bar{u}_{avg}}dx, \quad \text{where } \bar{u}_s = f(\bar{x}). \tag{33}$$

2.3.2. Section B

Section B is modeled entirely by flow through an open rectangular channel, which is Eq. (24) with $\bar{u}_b = 0$ for no-slip boundary conditions. The superficial velocity U is once again Eq. (25), where the average velocity $\bar{u}_{avg}$ is found by integrating Eq. (24) with $\bar{u}_b$ set to zero. The original model by Zhang et al. (2010) used a constant area-averaged channel width:

$$w_{eff,Zhang} = \frac{ld - d^2\pi/4}{d} = l - \frac{d\pi}{4}, \tag{34}$$

but in reality the width available for flow follows the shape of the pillar surface and varies as function of x. As an improvement to the model, w_{eff} now goes from l at the edge of section B to w at the center, and then returns to l at the opposite edge. Using a polar coordinate transformation:

$$w_{eff} = l - d\sqrt{1 - (x/(d/2))^2}, \tag{35}$$

where x goes from $-d/2$ to $d/2$. Recognizing that $\bar{u}_{avg}$ and w_{eff} are both functions of x, integrating Eq. (25) from $-d/2$ to $d/2$ gives the pressure drop for section B in a single cell. Scaling by the total number of cells results in:

$$\Delta P_B = \frac{2\mu}{h^2}\frac{l}{s+d}LU\int_{-d/2}^{d/2}\left(\frac{1}{w_{eff}\bar{u}_{avg}}\right)dx. \tag{36}$$

2.3.3. Total permeability

The overall permeability for the micropillar array is

$$K_{total} = \frac{U\mu}{\Delta P_{total}/L}, \tag{37}$$

and ΔP_{total} is equal to the sum of ΔP_A and ΔP_B. Remembering that $K^* = K/d^2$, the total dimensionless permeabilities are presented below. Eq. (38) uses the fully-developed flow assumption ($\bar{u}_s = 1$) for section A, Eq. (39) uses a zero boundary velocity ($\bar{u}_s = 0$), and Eq. (40) uses a varying boundary velocity profile ($\bar{u}_s = f(\bar{x})$).

$$K^*_{total,(\bar{u}_s=1)} = \left[3\left(\frac{d}{h}\right)^2\frac{s}{s+d} + \frac{\int_{\frac{-d}{2}}^{\frac{d}{2}}\frac{1}{\bar{u}_{avg}w_{eff}}dx}{\frac{1}{2}\left(\frac{h}{d}\right)^2\frac{s+d}{l}}\right]^{-1} \tag{38}$$

$$K^*_{total,(\bar{u}_s=0)} = \left[\frac{2s}{s+d}\left(\frac{d}{h}\right)^2\frac{1}{\bar{u}_{avg}} + \frac{\int_{\frac{-d}{2}}^{\frac{d}{2}}\frac{1}{\bar{u}_{avg}w_{eff}}dx}{\frac{1}{2}\left(\frac{h}{d}\right)^2\frac{s+d}{l}}\right]^{-1} \tag{39}$$

$$K^*_{total,(\bar{u}_s=f(\bar{x}))} = \left[\frac{2}{s+d}\left(\frac{d}{h}\right)^2\int_d^{s+d}\frac{1}{\bar{u}_{avg}}dx + \frac{\int_{\frac{-d}{2}}^{\frac{d}{2}}\frac{1}{\bar{u}_{avg}w_{eff}}dx}{\frac{1}{2}\left(\frac{h}{d}\right)^2\frac{s+d}{l}}\right]^{-1} \tag{40}$$

Similar to Eq. (15), Eqs. (38)–(40) are written in terms of separate x- and y-direction pillar spacings. This study concentrates on square arrays where the x- and y- spacings are equal and briefly explores

rectangular arrays. The proposed model provides a basic and straightforward tool that can be utilized to study rectangular pillar arrangements in more depth in the future.

2.4. Numerical simulation

Numerical simulations allow for 3-D velocity profile modeling and provide a unique benefit due to their ability to specify a periodic boundary condition instead of a velocity boundary condition. Ranjan et al. (2012) recently used FLUENT® to calculate permeabilities of cylindrical pillar arrays as a function of porosity. Similarly, Srivastava et al. (2010) used COMSOL V3.5a (COMSOL, Inc., Stockholm, Sweden) to determine the dependence of a dimensionless fluid flow rate through square pillar arrays on two dimensionless geometric parameters: h/w and w/d. The simulation used a unit cell approach, and the boundary conditions were no-slip on solid surfaces, pressure constraints on upstream and downstream cell faces, and symmetric profiles on all other faces. The resulting dimensionless flow rate per unit width $\hat{q}$ is:

$$\hat{q} = \frac{3\mu q}{\left(\frac{dP}{dx}\right) l d^2} = \left(\frac{1}{10}\right)\left(\frac{h}{w}\right)^{1.17}\left(\frac{w}{d}\right)^{2.5}, \tag{41}$$

where q is the dimensional flow rate per unit width. Eq. (41) is accurate to within 10% for 5 μm $\leqslant d \leqslant$ 100 μm, $1 \sim w/d \sim 10$, and $1 < h/w < 10$. Rearranging Eq. (41) to solve for the average dimensionless velocity and thus the dimensionless permeability as defined by Eq. (1) gives

$$K_S^* = \frac{1}{30}\left(\frac{l}{h}\right)\left(\frac{h}{w}\right)^{1.17}\left(\frac{w}{d}\right)^{2.5}. \tag{42}$$

We performed our own COMSOL simulations both to explore ranges of h/w and w/d above 10 and to validate Eq. (42). The bottom surface and pillar walls were specified no-slip. The top surface had a symmetry boundary condition, and the surfaces at $y = 0$ and $y = l$ had periodic flow conditions. Instead of using periodic conditions for the inlet and oulet, laminar flow inlet and outlet pressures were specified. To eliminate entrance and exit effects, we extended the simulation from a single cell to an array ten cells long and one cell wide. The resulting superficial velocity and pressure distributions were measured and used to calculated the Darcy permeability for each cell. The permeabilities from the center cells were averaged to give the final permeability with ⩽1% uncertainty on the average. Fig. 5 shows a schematic of the simulation domain and corresponding boundary conditions for a single cell, and Fig. 6 shows a 3-D rendering of an example velocity profile for an entire array.

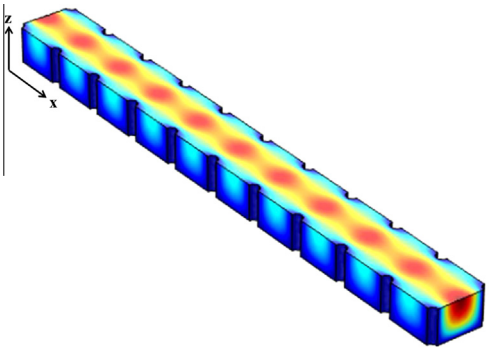

Fig. 6. 3-D COMSOL velocity profile through micropillar array to demonstrate computation domain. h = 90 μm, d = 30 μm, $l = S$ = 150 μm.

2.5. Model comparisons

The dimensionless permeabilities of the fluid flow models just described are summarized in Table 1 for square pillar arrangements in terms of two dimensionless geometric groups: $\phi_1 = h/d$ and $\phi_2 = l/d$. The last seven equations in Table 1 model actual pillar arrays, and Fig. 7 shows four of these dimensionless permeabilities vs. ϵ (Eq. (6)) for two ratios of h/d. Numerical simulation results from Srivastava et al. (2010) are not shown because of their limited applicability range; however, the COMSOL results obtained for this study are included as K_C^*. The three solutions of the author's model are almost identical at low values of porosity, so only the varying boundary velocity result is shown in Fig. 7.

At low porosities, the true system follows the lubrication solution for a cylinder bank (Gebart, 1992). The permeability proposed by Yazdchi et al. (2011) recognizes this transition and matches the solution by Gebart (1992) at low porosities. Although the model developed by the present authors does not follow an exact lubrication solution, it accounts for the varying flow area caused by the curved pillar surfaces. Consequently, the authors' solution matches the other models well at low porosities.

For the applications of interest here, h, d, and w vary between 5 μm and 200 μm. The majority of pillar arrays within those dimensions have $\epsilon > 0.9$. Therefore, Fig. 8 plots permeabilities against the more representative scale of l/d. COMSOL results from Srivastava et al. (2010) are plotted only where the model is applicable. The analytical permeabilities of the pillar array with $h/d = 0.25$ and $h/d = 0.5$ approach that of a flat plate at high porosities, which is expected since the pillars are short and far apart. The authors' model has an advantage over Tamayol and Bahrami (2009) and the Brinkman model in that it is the only analytical model that takes into account the 2-D velocity effects of the flat

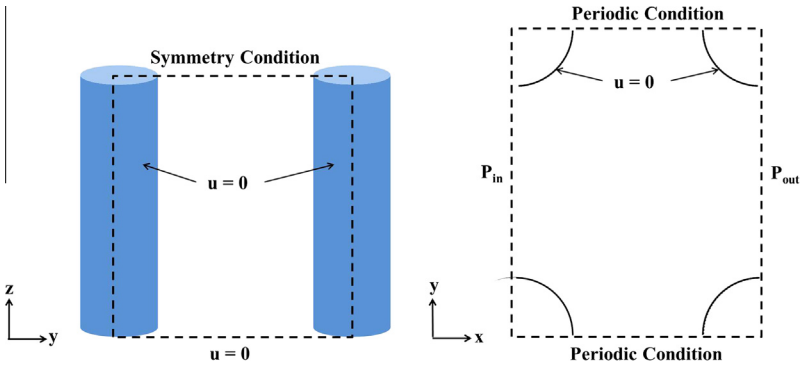

Fig. 5. Computation domain (dashed line) and boundary conditions used in the numerical model to simulate fluid flow through a micropillar array. Left and right schematics are side and top views of a single cell, respectively.

Table 1
Dimensionless permeabilities in terms of $\phi_1 = h/d$ and $\phi_2 = l/d$ for different fluid flow models through micropillar arrays.

Author	K^*	Comments
Flat plate	$K^*_{plate} = \frac{1}{3}\phi_1^2\left(1 - \frac{\pi}{4}\phi_2^{-2}\right)$	Flat plate with air interface
Gebart (1992)	$K^*_{G,cyl} = \frac{4}{9\pi\sqrt{2}}(\phi_2 - 1)^{5/2}$	Square cylinder bank
Drummond and Tahir (1984)	$K^*_{D,cyl} = \frac{1}{32\phi}\left(\ln(\frac{1}{\phi}) - 1.476 + \frac{2\phi - 0.796\phi^2}{1+0.489\phi-1.605\phi^2}\right)$, where $\phi = \frac{\pi}{4}\phi_2^{-2}$	Square cylinder bank
Yazdchi et al. (2011)	$K^*_{Y,cyl} = \frac{K^*_{G,cyl}}{1+0.336(\pi/4-\phi)} + \left(K^*_{D,cyl} - \frac{K^*_{G,cyl}}{1+0.336(\pi/4-\phi)}\right)\frac{1+tanh(\frac{0.25-\phi}{0.037})}{2}$	Square cylinder bank
Tamayol and Bahrami (2009)	$K^*_{T,cyl} = \left\{\frac{18+12(\phi_2^2-1)}{(1-\phi_2^2)^2\phi_2} + \frac{18\phi_2\left[\arctan\left(\frac{1}{\sqrt{\phi_2^2-1}}\right)+\pi/2\right]}{(\phi_2^2-1)^{5/2}} + \frac{12(\phi_2-1)}{\phi_2^3}\left[\frac{2-g(\phi_2)}{2}\right]\right\}^{-1}$	Square cylinder bank
	where $g(\phi_2) = 1.274(1 - \frac{\pi}{4}\phi_2^{-2}) - 0.274$	Square cylinder bank
Yazdchi et al. (2011) Total	$K^*_{Y,total} = \left(\frac{1}{K^*_{Y,cyl}} + \frac{1}{K^*_{plate}}\right)^{-1}$	Combined cyl. bank and plate
Tamayol and Bahrami (2009) Total	$K^*_{T,total} = \left(\frac{1}{K^*_{T,cyl}} + \frac{1}{K^*_{plate}}\right)^{-1}$	Combined cyl. bank and plate
Brinkman Xiao et al. (2010)	$K^*_B = K^*_{Y,cyl} - \frac{(K^*_{Y,cyl})^{3/2}}{\phi_1\sqrt{1-\frac{\pi}{4}\phi_2^{-2}}}\tanh\left(\frac{\phi_1}{\sqrt{K^*_{Y,cyl}}}\sqrt{1-\frac{\pi}{4}\phi_2^{-2}}\right)$	Pillar array
Author model ($u_s = 1$: Eq. (38))	$K^*_{total,(u_s=1)} = \left\{3\frac{\phi_2-1}{\phi_1^2\phi_2} + \left(\int_{\frac{1}{2\phi_1}}^{\frac{1}{2\phi_1}}\frac{h}{\bar{u}_{avg}w_{eff}}d(x/h)\right)\left(\frac{2}{\phi_1^2}\right)\right\}^{-1}$	Pillar array
Author model ($u_s = 0$: Eq. (39))	$K^*_{total,(\bar{u}_s=0)} = \left\{\frac{2(\phi_2-1)}{\phi_1^2\phi_2}\frac{1}{\bar{u}_{avg}} + \left(\int_{\frac{1}{2\phi_1}}^{\frac{1}{2\phi_1}}\frac{h}{\bar{u}_{avg}w_{eff}}d(x/h)\right)\left(\frac{2}{\phi_1^2}\right)\right\}^{-1}$	Pillar array
Author model ($\bar{u}_s = f(\bar{x})$: Eq. (40))	$K^*_{total,(\bar{u}_s=f(\bar{x}))} = \left\{\frac{2}{\phi_1^2\phi_2}\int_1^{\phi_2}\frac{1}{\bar{u}_{avg}}d(x/d) + \left(\int_{\frac{1}{2\phi_1}}^{\frac{1}{2\phi_1}}\frac{h}{\bar{u}_{avg}w_{eff}}d(x/h)\right)\left(\frac{2}{\phi_1^2}\right)\right\}^{-1}$	Pillar array
Srivastava et al. (2010)	$K^*_S = \frac{1}{30}\left(\frac{\phi_2}{\phi_1}\right)\left(\frac{\phi_1}{\phi_2-1}\right)^{1.17}(\phi_2 - 1)^{2.5}$	Numerical sim. of pillar array

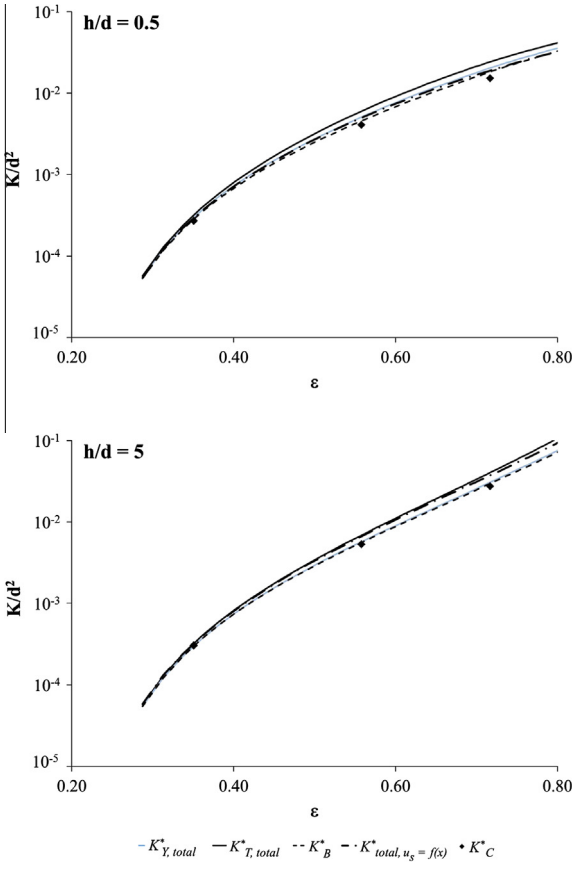

Fig. 7. Dimensionless permeability vs. 2-D porosity for a square micropillar array with $h/d = 0.5$ (top) and 5 (bottom).

bottom in the pillar section. This difference is not critical at high h/d ratios, where the flat bottom surface effects are small compared to the pillar surface effects. However, at low h/d, the flat bottom has a significant effect on the overall permeability, as seen in Fig. 8 for $h/d = 0.25$ and $h/d = 0.5$. Thus neglecting the 2-D effects of the velocity profile at the transition between the pillar wall and flat bottom is a potential reason that the other analytical models overestimate the permeability for short pillar geometries. The COMSOL results remain consistently below the value for a flat plate, even at high porosities. Further study of the COMSOL velocity profile for $h/d = 0.5$ revealed that at high l/d ratios, the flow rate becomes high and leads to developing flow conditions in the pillar regions. This produces shear rates higher than predicted by the authors' model. The numerical simulations reflect intricate developing effects, and the authors' model attempts to accommodate those conditions with a variable boundary velocity. At low h/d, the authors' model performs the best out of all the models presented.

As h/d increases, the pillar height becomes more prominent and the permeabilities appear like those of a cylinder bank. The values of $K^*_{Y,total}$, K^*_B, and K^*_S are numerically similar for all ratios of h/d, but $K^*_{T,total}$ is consistently higher. The Brinkman model matches previous simulation results by Srivastava et al. (2010), but COMSOL results from this study indicate that the Brinkman model deviates at high l/d. The long-range permeability behavior at $l/d > 15$ (not shown) is that all of the models approach the fully developed flow assumption (uniform velocity). This is to be expected, considering that the pillars are far apart and so most of section A is fully developed flow.

COMSOL and the authors' models represent the micropillar system most realistically because they account for the cylindrical and flat surfaces of a pillar array simultaneously instead of relying on weighting methods or approximate geometries. The solutions of the current authors' model for $u_s = 1$ and $u_s = 0$ (Eqs. (38) and (39)) delineate the upper and lower bounds of permeability for the model. These solutions are not shown because the varying boundary velocity solution (Eq. (40)) is a more accurate midrange solution between the two. The boundary velocity solution matches numerical results well for $h/d = 5$ and with acceptable accuracy for $h/d = 2$. The authors' varying boundary velocity model thus captures the important physics of fluid flow in micropillar arrays.

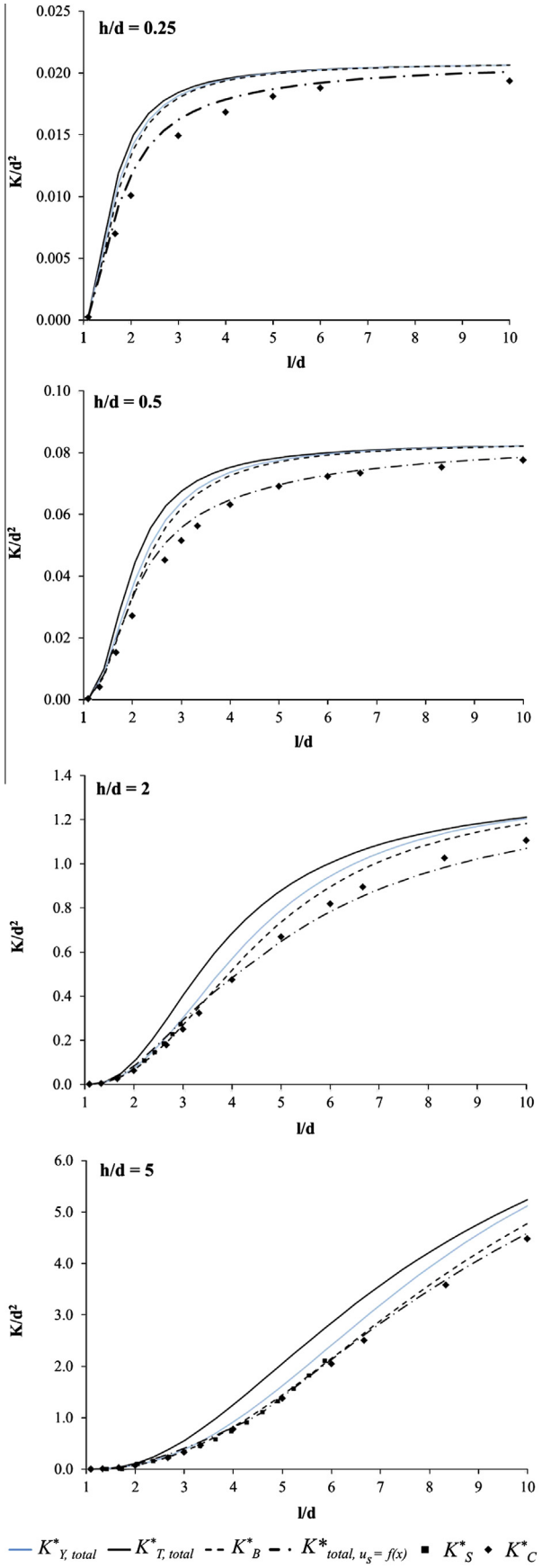

Fig. 8. Dimensionless permeability vs. $\phi_2 = l/d$ for a square micropillar array with $h/d = 0.25$, 0.5, 2, and 5.

Interestingly, the accuracy of the analytical models depends on h/d. Based on additional results for $h/d = 10$ (not shown), the Brinkman model becomes more accurate (as compared to COMSOL results) as h/d increases, whereas the varying boundary velocity hits a maximum accuracy around $h/d = 5$. There is clearly a relationship between permeability and height that is not being accounted for in either model. Numerical results have indicated that the real flow involves developing velocity profiles and a complex dependence on pillar height beyond the capabilities of the current models. For exact solutions of square pillar arrangements, the authors' model provides the robustness and accuracy needed for design work up to $h/d = 5$. At the higher flowrates observed at $h/d > 5$, the authors' model does not capture all of the flow patterns observed numerically. The Brinkman equation overestimates the results at low h/d and is better suited for $h/d > 5$, where the flat bottom effects are small compared to the pillar surface effects. Therefore, we can create a hybrid permeability that uses the varying boundary velocity model for $h/d \leqslant 5$ and the Brinkman model for $h/d > 5$.

The authors' model has another key area of strength. The Brinkman equation is less ideal for the exploration of unconventional geometries because it requires a cylinder bank permeability term, and Tamayol and Bahrami (2009) are among the few who have extended their analyses past homogeneous square or hexagonal banks. COMSOL simulations can be adapted to different geometries once the user has acquired sufficient software expertise, but the current authors' solution offers an analytical model capable of handling alternate geometries easily and quickly. So, alternate geometries can be modeled either with COMSOL simulations, the Brinkman equation using the permeability of Tamayol and Bahrami (2009) as the cylinder bank permeability, or the authors' model. Fig. 9 shows the permeability of pillar arrays arranged in rectangular configurations, where S/d is constant but l/d is varied. The Brinkman equation result K^*_B now uses the cylinder bank permeability from Tamayol and Bahrami (2009) instead of Yazdchi et al. (2011).

The authors' solution matches closely to COMSOL results for $S/d \leqslant 3$. The Brinkman equation provides less accurate results, potentially stemming from the fact that the solution proposed by Tamayol and Bahrami (2009) uses different approximations for the velocity profile in the cylinder banks. Small S/d ratios are advantageous to heat pipes because they create high capillary pressures, which will be discussed in the next section. Therefore, the authors' model is clearly useful for predicting the permeabilities of pillar arrays in rectangular geometries and requires less time and expertise than numerical simulations.

3. Capillary pressure gradient

Fluid flow in capillary wicking devices is a competition between the driving capillary pressure gradient and viscous losses. The previous section explored different models for the viscous losses in a micropillar array. However, the appropriate capillary pressure gradient depends upon the application of the wick. Many experimentalists test the wicking capabilities of new materials by performing a rate-of-rise experiment, which tracks the propagation of a fluid front through an unwetted material (Srivastava et al., 2010; Xiao et al., 2010; Nam et al., 2010). The pressure gradient for these systems depends on the surface energy difference between wet and dry portions of the wick. In contrast, heat pipe wicks are continuously wetted. This section presents the capillary pressure gradient for a micropillar array used as a heat pipe wick.

The capillary pressure difference over a vapor–liquid interface is (Peterson, 1994)

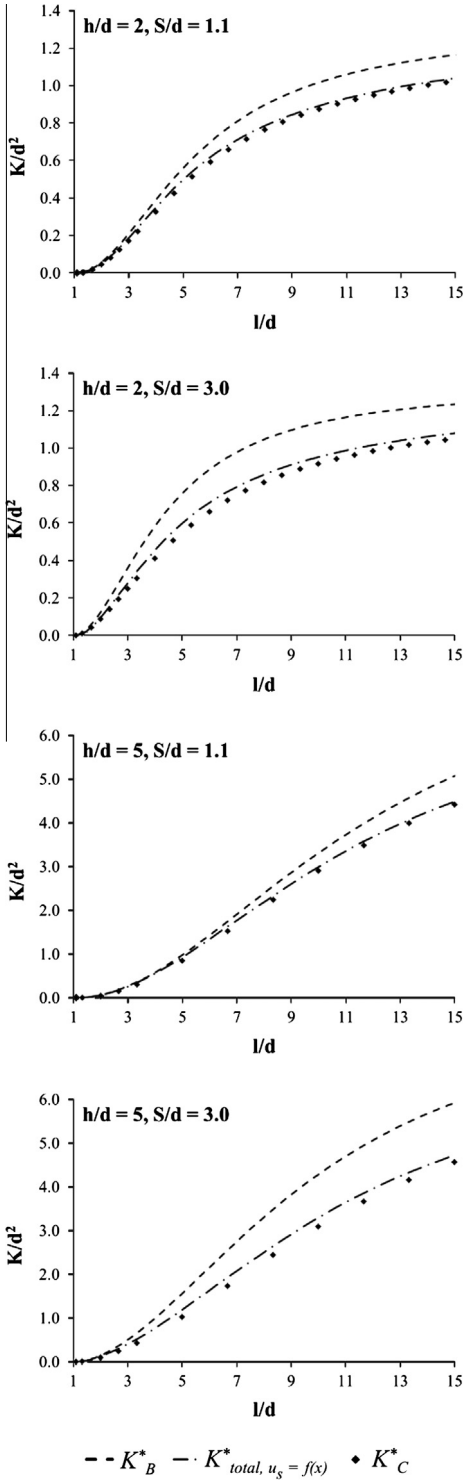

Fig. 9. Dimensionless permeability vs. $\phi_2 = l/d$ for a rectangular micropillar array with $h/d = 2$, $S/d = 1.1$ (top left), $h/d = 2$, $S/d = 3$ (top right), $h/d = 5$, $S/d = 1.1$ (bottom left), and $h/d = 5$, $S/d = 3$ (bottom right). K_B^* uses the cylinder bank permeability from Tamayol and Bahrami (2009).

$$P_v - P_l = \sigma\left(\frac{1}{R_1} + \frac{1}{R_2}\right), \tag{43}$$

where P_v is the vapor pressure, P_l is the liquid pressure, σ is the liquid/vapor surface tension, and R_1 and R_2 are the principle radii of curvature of the liquid meniscus. The principle radii of curvature are assumed to be equal for square pillar arrays due to geometric symmetry, so

$$P_v - P_1 = \frac{2\sigma}{R}. \tag{44}$$

In a heat pipe, the difference between the capillary pressures in the evaporator and condenser sections drives fluid flow through the wick:

$$\Delta P_{cap} = \frac{2\sigma}{R_{evap}} - \frac{2\sigma}{R_{cond}}. \tag{45}$$

Vaporization in the evaporator causes the liquid meniscus to recede, while condensation submerges the wick in the condenser section and causes $R_{cond} \to \infty$. The principle radius in the evaporator is related to the contact angle of the liquid with the wicking surface, θ, and the effective radius of the wick pores, r_{eff} (Peterson, 1994). Therefore, the capillary pressure becomes

$$\Delta P_{cap} = \frac{2\sigma\cos\theta}{r_{eff,evap}}. \tag{46}$$

The contact angle must be low enough for the liquid to wet the surface of the pillars (a threshold explored by Priest et al. (2012)), but maximum fluid flow through the wick is achieved when the liquid completely wets the wick ($\theta = 0$). For wire screens, the effective radius of curvature is $0.5(w + d_w)$, where w is the wire spacing and d_w is the wire diameter. However, Nam et al. (2010) tested hexagonal pillar arrays and found that the effective pore radius did not change significantly with pillar diameter, but instead changed with pillar spacing. This indicates that the correct effective radius for square pillar arrays is $0.5w$, not $0.5(w + d)$. Thus, a first approximation for the maximum driving capillary pressure for a micropillar wick in a heat pipe is

$$\Delta P_{cap,max} = \frac{4\sigma}{w}. \tag{47}$$

For non-symmetric pillar geometries, the capillary pressure can be expressed in terms of w and s:

$$\Delta P_{cap,max} = \sigma\left(\frac{2}{s} + \frac{2}{w}\right). \tag{48}$$

One point to note is that this equation assumes that the liquid contact line is pinned at the top pillar edge, while in reality the curvature will be less severe. The extent to which Eq. (48) overestimates the capillary pressure could be known through a more rigorous surface energy analysis, but that is beyond the scope of this project.

4. Flow rate calculations

The cooling capacity of heat pipes is related to the mass flow rate of liquid through the internal wick, and we are interested in comparing wicks on the basis of their best-case scenario even though heat pipes do not always operate at full capacity. The capillary pressure can be non-dimensionalized as follows:

$$\Delta P_{cap}^* = \frac{\Delta P_{cap,max}\, d}{\sigma}. \tag{49}$$

To explore the relationship between pillar geometry and maximum flow rate, the dimensionless velocity is:

$$U^* = K^* \Delta P_{cap}^*. \tag{50}$$

The mass flow rate through the wick can easily be derived from the velocity by multiplying by cross-sectional area and fluid density:

$$\dot{m} = U^*\left(\frac{\rho\sigma}{\mu}\frac{A_c d}{L}\right), \tag{51}$$

where $\dot{m}$ is the dimensional mass flow rate, L is the macroscopic wick length, $A_c = hW$ is the superficial cross-sectional wick area, and ρ is the fluid density. U^* is a function of h/d and l/d alone, so a parameter sweep can determine where the maximum flow rate occurs. The results are shown in Figs. 10 and 11. Fig. 10 is a contour plot of U^* vs. h/d and l/d, and Fig. 11 shows U^* vs. l/d for three different h/d ratios. The top right contour plot is a hybrid between the authors' model and the Brinkman equation. The authors' model (Eq. (40)) is used for $h/d \leqslant 5$ due to its superior accuracy at low pillar heights, and the Brinkman equation is used for $h/d > 5$. The contour plot lines corresponding to COMSOL results (U_C^*) are not completely smooth because they are generated from a set of 198 evenly spaced combinations of h/d and l/d.

Fig. 11 shows that the authors' model kinks at the transition from a zero boundary velocity to a finite boundary profile, as indicated in Eq. (28), but overall the model matches well to numerical results for $h/d \leqslant 5$. All of the models exhibit the same trend: for a given h/d, the dimensionless mass flow rate initially increases with pillar spacing due to decreased viscous losses. However, the simultaneous decrease in $\Delta P_{cap,max}$ causes the flow rate to reach a maximum and then decrease with continued pillar spacing increases. Therefore, there is an optimal l/d at a given h/d; this optimum occurs at the inflection point of each contour line in Fig. 10. The relationship between h/d and the inflection point l/d is approximately linear for each model, and the equations are given in Table 2. The R^2 values represent the coefficient of determination for each linear fit based on standard linear regression techniques.

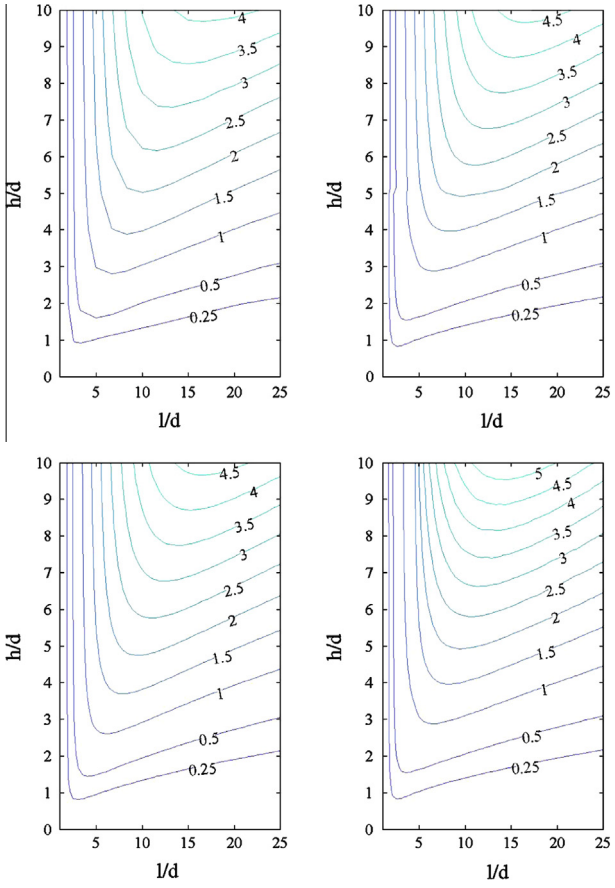

Fig. 10. Contour plot of dimensionless velocity vs. h/d and l/d for different permeability models. COMSOL results – U_C^* – top left, a hybrid between Eq. (40) and U_B^* – top right, Brinkman equation – U_B^* – bottom left, and varying boundary velocity – $U^*_{total,(\bar{u}_s=f(\bar{x}))}$ – bottom right.

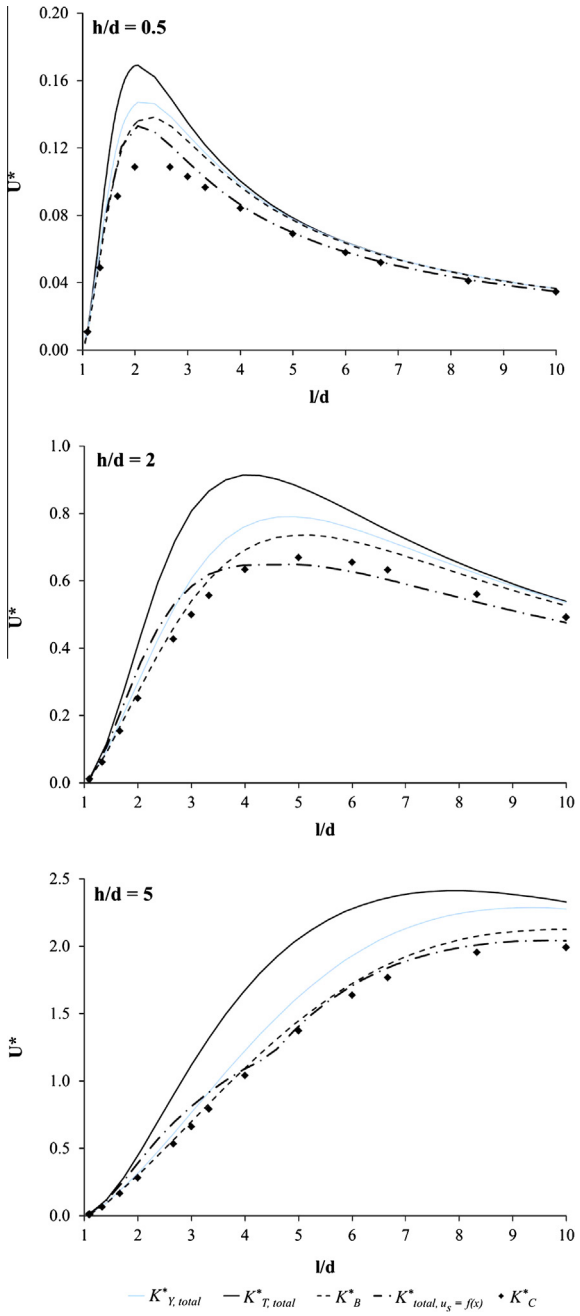

Fig. 11. Dimensionless mass flow rate vs. l/d for different permeability models with $h/d = 0.5$, 2, and 5.

Table 2
Curve fit of inflection point l/d to h/d for several permeability models.

Model	Equation	R^2
COMSOL simulations	$(l/d)_{inf} = 1.526\left(\frac{h}{d}\right) + 1.907$	0.996
Xiao et al. (2010)	$(l/d)_{inf} = 1.488\left(\frac{h}{d}\right) + 2.311$	0.998
Boundary Vel. ($h/d < 5$)	$(l/d)_{inf} = 1.720\left(\frac{h}{d}\right) + 1.272$	0.991
Boundary Vel. ($h/d > 5$)	$(l/d)_{inf} = 0.974\left(\frac{h}{d}\right) + 4.985$	0.990

The real strength of the authors' model is for rectangular pillar geometries, particularly at low S/d. Fig. 12 shows these results by plotting dimensionless velocity for both square and rectangular pillar geometries on a logarithmic scale. The authors' model fits

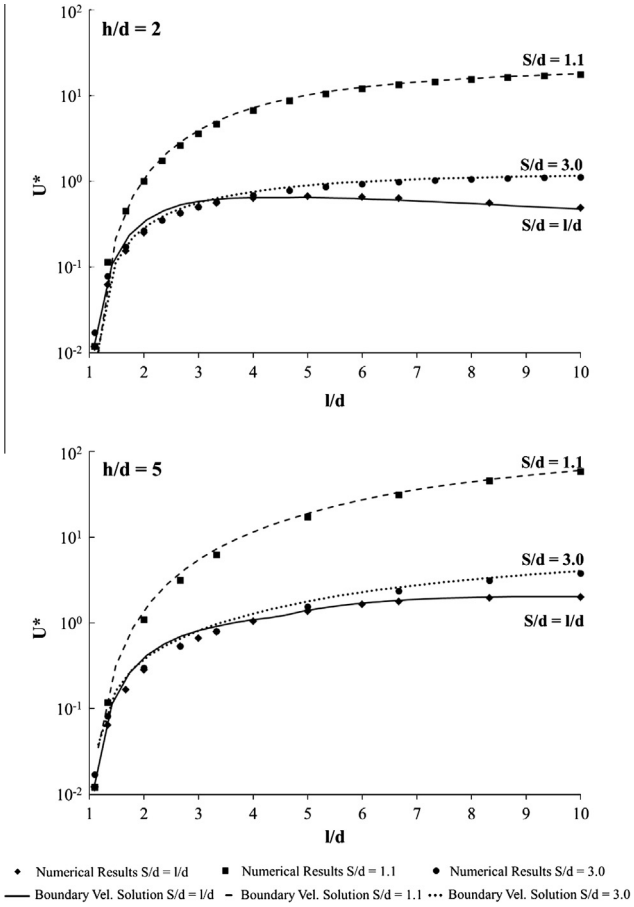

Fig. 12. Dimensionless velocity vs. $\phi_2 = l/d$ for both square and rectangular micropillar arrays with $h/d = 2$ (top) and $h/d = 5$ (bottom).

well to numerical results. In addition, rectangular arrays demonstrate potential for larger flow rates than square arrays. Eq. (48) shows that the capillary pressure has the same theoretical dependence on both S/d and l/d. As permeability increases with l/d, the capillary pressure also stays high due to the fact that S/d is constant. So, Fig. 12 indicates that micropillar arrays could be designed to benefit from increased permeability without sacrificing capillary pressure. With $S/d = 1.1$, the dimensionless velocity is at least an order of magnitude higher than a square array for a given l/d. The velocity drops dramatically when S/d increases to 3 due to the inverse dependence of capillary pressure on spacing. This suggests that the largest benefits of rectangular arrays are realized at small S/d. More study is needed on the exact dependence of the capillary pressure on individual $l-$ and $S-$ spacings to ensure that the surface radii of curvature within rectangular pillar configurations can still be represented by Eq. (48).

For both square and rectangular arrangements, there is not an optimum h/d at which the flow rate peaks for a given l/d value. Instead, the contour plots indicate that the flow rate just continuously increases as h/d increases, so that the global maximum flow rate occurs at the highest h/d possible. This is mathematically true since the flow rate reflects the balance of the flat plate and cylinder bank aspects of the array. When the pillars are short or spread apart (low h/d or high l/d), the array behaves more like a flat plate, so flow rate increases with h/d. Unfortunately, the benefit of increasing h/d is accompanied by the array behaving more like a cylinder bank. Under those conditions, the flow rate increases primarily with pillar spacing until the inflection point is reached. Past the inflection point, the array begins to look like a flat plate again so flow rate once again increases wih h/d. This leads to the behavior in Fig. 10, where it seems beneficial to increase h/d and l/d infinitely. There are two reasons that this conclusion is not realistic. First, the equation for capillary pressure (Eq. (43)) loses validity when the liquid–vapor interface is no longer dictated by surface tension effects. Fig. 10 shows that the contour inflections will eventually move into an l/d region where the liquid between the pillars does not actually create a capillary pressure because the pillar spacing exceeds the capillary length. The capillary length is the point at which gravity becomes the dominant force on the fluid meniscus shape instead of surface tension. For the proposed models to apply, the surface tension effects should be at least an order of magnitude larger than the hydrostatic effects so that h and l are both $< \sqrt{0.1\sigma/\rho g}$, or $Bo = (\rho g\ h\ l/\sigma) < 0.1$, where Bo is the Bond number. Second, manufacturing constraints create limits on pillar dimensions irrespective of capillary pressure. Pillars with small aspect ratios or large heights are difficult to create, and careful consideration as to their stability is required (Chandra and Yang, 2010), although nano and micromanufacturing advances continue to push modern capability limits. Taking these two limiting factors into account, the global maximum mass flow rate for micropillar heat pipe wicks occurs at the highest h/d allowed by manufacturing that still results in a Bond number less than 0.1 at the corresponding optimum l/d.

5. Cooling capacity predictions for square arrays

In heat pipes, the purpose of increasing the fluid flow rate through the internal wick is to raise the maximum heat transfer capacity of the pipe (*i.e.* the capillary limit). This section determines the pillar dimensions necessary to achieve 1000 W/cm^2 of maximum cooling capacity. Only square arrays are considered since they are the main focus of this study. The model used is a hybrid between the authors' model and the Brinkman equation. Eq. (40) was used for $h/d \leqslant 5$, and the Brinkman model using the permeability by Yazdchi et al. (2011) was used for $h/d > 5$. Wang and Bar-Cohen (2007) found that local hot spots on microprocessors typically produced heat fluxes of 680 W/cm^2. In addition, Tuckerman and Pease (1981) created a compact, water-cooled heat sink capable of dissipating 790 W/cm^2 but predicted that 1000 W/cm^2 should be possible. Therefore, 1000 W/cm^2 was the target cooling capacity used in this study. The cooling capacity of a wick is given by: $Q = \dot{m} h_{vap}$, where Q is the total heat transfer and h_{vap} is the heat of vaporization of the working fluid. One of the three pillar dimensions must be specified to calculate $\dot{m}$ according to Eq. (50). The authors evaluated three test cases where $d = 10$, 50, and 100 μm. The model fluid was water, and Table 3 gives the physical parameters used in the analysis. The macroscopic wick dimension was 1×3 cm, and the evaporator surface area was 1 cm^2.

Fig. 13 shows the contour plots of $\dot{m}$ vs. l and h for the three wicks. The dotted line in Fig. 13 represents the mass flow rate needed to transfer 1000 W/cm^2 of heat, assuming no environmental losses. All three pillar diameters can achieve 1000 W/cm^2 of cooling without exceeding the capillary length, since $l_{cap} = 2600$ μm for water. However, the pillar height is a more substantial issue.

Table 3
Physical system parameters used to calculate mass flow rates.

Parameter	Value	Description
σ	0.066 N/m	Liquid–vapor surface tension
ρ	983.3 kg/m^3	Liquid density
μ	0.463×10^{-3} Ns/m^2	Liquid viscosity
h_{vap}	2260 J/g	Heat of vaporization
L	0.03 m	Macroscopic wick length
W	0.01 m	Macroscopic wick width

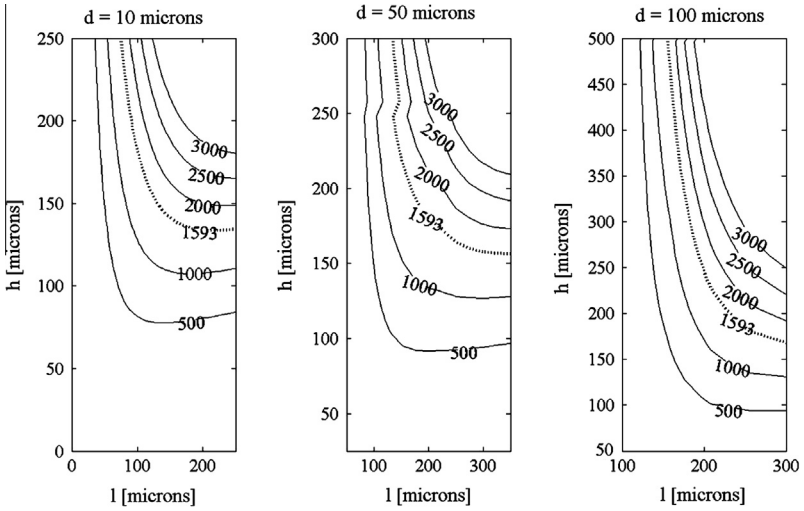

Fig. 13. Mass flow rate in g/h vs. l and h for d = 10 μm (left), 50 μm (center), and 100 μm (right). Dotted line indicates the mass flow rate needed to dissipate 1000 W/cm^2 via fluid vaporization.

Pillars with 10 μm diameters require high aspect ratios to meet the desired goal, which decreases the mechanical stability of the pillars. However, 100 μm-diameter pillars require large absolute values for pillar height, which increases manufacturing difficulty. Therefore, manufacturing considerations suggest that midrange diameters are the most desirable for micropillar wicks.

Fig. 13 in combination with Fig. 10 creates a powerful design tool that maps out the effects of h, d, and l on the maximum mass flow rate through micropillar wicks. Once one of the three geometric parameters is fixed based on design criteria, Fig. 13 provides a convenient and fast method to tune the remaining two parameters to produce the desired maximum amount of heat dissipation. Fig. 13 is specific to the experimental parameters given in Table 3 but is derived from Fig. 10, which can be used as a foundation for other test cases.

The wick length also plays a significant role in wick performance. The capillary limit decreases as the wick lengthens due to increased viscous resistance without corresponding gains in capillary pressure. Therefore, the benefits of micropillar wicks are best realized at short heat pipe lengths. Recent interest in on-chip cooling technologies provide a potential application, where high spot cooling capacity is a necessity but the wicks only need to be long enough to reach the heat sink (Wang and Bar-Cohen, 2007).

6. Conclusions

Fluid flow through micropillar arrays has shown promise in a variety of technological fields, and the permeability of these arrays is a key parameter in their design and application. In this paper we evaluated several permeability models to identify a robust model for optimizing pillar dimensions for a given application. Numerical simulations were performed to provide the most complete solutions for all pillar configurations, but the simulation process required time and careful attention to ensure that the results were accurate. Analytically, models that combined cylinder bank and flat plate permeabilities exhibited the expected behavior with acceptable numerical accuracy. The Brinkman equation matched numerical simulations most closely for pillars arranged in square arrays with high h/d. Finally, a 2-D velocity solution with varying boundary conditions matched well to respected models at low porosities; at high porosities this approach provided comparable or superior results up to $h/d = 5$. Therefore, a hybrid model was created to combine the strengths of both models by using the 2-D velocity solution for $h/d \leqslant 5$ and the Brinkman equation for $h/d > 5$. To explore alternative pillar arrangements, the Brinkman equation would require the permeability of the corresponding cylinder bank, for which there is at least one model available (Tamayol and Bahrami, 2009). However, the current authors' model is easily adapted to rectangular pillar arrangements and accounts for the unique velocity profile at the intersection of bottom surface and the pillar wall, making it a viable alternative to numerical simulations. Indeed, several results for rectangular arrays were presented and indicated that the authors' model achieved the closest match to simulations out of all the available models at low pillar spacings.

We also optimized micropillar wick dimensions for maximum fluid flow rate in heat pipe applications. The capillary pressure for a heat pipe applied to the micropillar array gave the insight that there is an optimal l/d for a given h/d based on the trade-off between viscous losses and capillary pressure that is not immediately apparent simply from pillar array permeability calculations. The figure of dimensionless flow rate vs. l/d and h/d given in this paper presents a convenient design tool to identify the combinations of pillar dimensions that give a desired maximum mass flow rate, and consequently a desired cooling capacity. In addition, preliminary results for alternative pillar configurations suggested that rectangular arrays could produce flow rates up to an order of magnitude higher than square arrays. The equation used to model the capillary pressure for rectangular arrays would need to be further improved to verify these results. Finally, three hypothetical test cases for wicks with d = 10, 50, and 100 μm indicated that 1000 W/cm^2 of maximum cooling capacity is achievable by all three diameters, but manufacturing capabilities suggest that midrange diameters are the most realistic option.

Acknowledgement

This work was performed at the University of Texas at Austin through the support of the National Science Foundation Chemical, Bioengineering, Environmental, and Transport Systems Grant 1134104.

References

Byon, C., Kim, S.J., 2011. The effect of meniscus on the permeability of micro-post arrays. J. Micromech. Microeng. 24, 115011.
Chandra, D., Yang, S., 2010. Stability of high-aspect-ratio micropillar arrays against adhesive and capillary forces. Acc. Chem. Res. 43, 1080–1091.
Cui, H.-H., Lim, K.-M., 2009. Pillar array microtraps with negative dielectrophoresis. Langmuir 25, 3336–3339.

de Beeck, J.O., Malsche, W.D., Tezcan, D.S., Moor, P.D., Desmet, G., 2012. Impact of the limitations of state-of-the-art micro-fabrication processes on the performance of pillar array columns for liquid chromatography. J. Chromatogr. A 1239, 35–48.
Deen, W., 1998. Analysis of Transport Phenomena. Oxford University Press Inc..
Drummond, J., Tahir, M.I., 1984. Laminar viscous flow through regular arrays of parallel solid cylinders. Int. J. Multiphase Flow 10, 515–540.
Gebart, B.R., 1992. Permeability of unidirectional reinforcements for RTM. J. Compos. Mater. 26, 1100–1133.
Ishino, C., Reyssat, M., Reyssat, E., Okumura, K., Quere, D., 2007. Wicking within forests of micropillars. Europhys. Lett. 79, 56005.
Lefevre, F., Lips, S., Rulliere, R., Conrardy, J., Raynaud, M., Bonjour, J., 2012. Flat plate heat pipes: from observations to the modeling of the capillary structure. Front. Heat Pipes 3, 013001.
Lips, S., Lefevre, F., Bonjour, J., 2010. Thermohydraulic study of a flat plate heat pipe by means of confocal microscopy: application to a 2D capillary structure. J. Heat Transfer 132, 112901.
Nagrath, S., Sequist, L.V., Maheswaran, S., Bell, D., Irimia, D., Ulkus, L., Smith, M., Kwak, E.L., Digumarthy, S., Muzikansky, A., Ryan, P., Balis, U.J., Tompkins, R.G., Haber, D.A., Toner, M., 2007. Isolation of rare circulating tumour cells in cancer patients by microchip technology. Nature 450, 1235–1239.
Nam, Y., Sharratt, S., Byon, C., Kim, S., Ju, Y., 2010. Fabrication and characterization of the capillary performance of superhydrophilic Cu micropost arrays. J. Microelectromech. S. 19, 581–588.
Peterson, G.P., 1994. An Introduction to Heat Pipes: Modeling, Testing, and Applications. John Wiley & Sons Inc..
Priest, C., Forsberg, P., Sedev, R., Ralston, J., 2012. Structure-induced spreading of liquid in micropillar arrays. Microsyst. Technol. 18, 167–173.
Ranjan, R., Patel, A., Garimella, S.V., Murthy, J.Y., 2012. Wicking and thermal characteristics of micropillared structures for use in passive heat spreaders. Int. J. Heat Mass Transfer 55, 586–596.
Sangani, A.S., Acrivos, A., 1982. Slow flow past periodic arrays of cylinders with application to heat transfer. Int. J. Multiphase Flow 8, 193–206.
Sharratt, S., Peng, C., Ju, Y.S., 2012. Micro-post evaporator wicks with improved phase change heat transfer performance. Int. J. Heat Mass Transfer 55, 6163–6169.
Sheng, W., Chen, T., Kamath, R., Xiong, X., Tan, W., Fan, Z.H., 2012. Aptamer-enabled efficient isolation of cancer cells from whole blood using a microfluidic device. Anal. Chem. 84, 4199–4206.
Shou, D., Fan, J., Ding, F., 2011. Hydraulic permeability of fibrous porous media. Int. J. Heat Mass Transfer 54, 4009–4018.
Song, Y., Noguchi, M., Takatsuki, K., Sekiguchi, T., Mizuno, J., Funatsu, T., Shoji, S., Tsunoda, M., 2012. Integration of pillar array columns into a gradient elution system for pressure-driven liquid chromatography. Anal. Chem. 84, 4739–4745.
Srivastava, N., Din, C., Judson, A., MacDonald, N.C., Meinhart, C.D., 2010. A unified scaling model for flow through a lattice of microfabricated posts. Lab Chip 10, 1148–1152.
Tamayol, A., Bahrami, M., 2009. Analytical determination of viscous permeability of fibrous porous media. Int. J. Heat Mass Transfer 52, 2407–2414.
Tamayol, A., Yeom, J., Akbari, M., Bahrami, M., 2013. Low Reynolds number flows across ordered arrays of micro-cylinders embedded in a rectangular micro/minichannel. Int. J. Heat Mass Transfer 58, 420–426.
Tuckerman, D., Pease, R., 1981. High-performance heat sinking for VLSI. IEEE Electr. Dev. Lett. 2, 126–129.
Vangelooven, J., Desmet, G., 2010. Theoretical optimisation of the side-wall of micropillar array columns using computational fluid dynamics. J. Chromatogr. A 1217, 8121–8126.
Wang, P., Bar-Cohen, A., 2007. On-chip hot spot cooling using silicon thermoelectric microcoolers. J. Appl. Phys. 102, 034503.
Xiao, R., Wang, E.N., 2011. Microscale liquid dynamics and the effect on macroscale propagation in pillar arrays. Langmuir 27, 10360–10364.
Xiao, R., Enright, R., Wang, E.N., 2010. Prediction and optimization of liquid propagation in micropillar arrays. Langmuir 26, 15070–15075.
Yazdchi, K., Srivastava, S., Luding, S., 2011. Microstructural effects on the permeability of periodic fibrous porous media. Int. J. Multiphase Flow 37, 956–966.
Yazdchi, K., Srivastava, S., Luding, S., 2012. Micro-macro relations for flow through random arrays of cylinders. Compos.: Part A 43, 2007–2020.
Zhang, C., Hidrovo, C.H., 2010. Characterization of capillary flow within a homogenously dispersed array of vertical micropillars. In: ASME Conference Proceedings 2010, pp. 655–663.